MNRAS 000, 1–16 (2016) Preprint 11 January 2017 Compiled using MNRAS LATEX style file v3.0

The HIX galaxy survey I: Study of the most gas rich galaxies from HIPASS

K. A. Lutz[1,2⋆], V. A. Kilborn[1], B. Catinella[3], B. S. Koribalski[2], T. H. Brown[1,3], L. Cortese[3], H. Dénes[2,4], G. I. G. Józsa[5,6,7] and O. I. Wong[3,8]

[1] *Centre for Astrophysics and Supercomputing, Swinburne University of Technology, P.O. Box 218, Hawthorn, VIC 3122, Australia*
[2] *Australia Telescope National Facility, CSIRO, P.O. Box 76, Epping, NSW 1710, Australia*
[3] *International Centre for Radio Astronomy Research (ICRAR), M468, The University of Western Australia, 35 Stirling Highway, Crawley, WA 6009, Australia*
[4] *Research School of Astronomy & Astrophysics, The Australian National University, Canberra, ACT 2611, Australia*
[5] *SKA South Africa Radio Astronomy Research Group, 3rd Floor, The Park, Park Road, Pinelands 7405, South Africa*
[6] *Rhodes Centre for Radio Astronomy Techniques & Technologies, Department of Physics and Electronics, Rhodes University, PO Box 94, Grahamstown 6140, South Africa*
[7] *Argelander-Institut für Astronomie, Auf dem Hügel 71, D-53121 Bonn, Germany*
[8] *ARC Centre of Excellence for All-Sky Astrophysics (CAASTRO)*

arXiv:1701.02447v1 [astro-ph.GA] 10 Jan 2017

Accepted XXX. Received YYY; in original form ZZZ

ABSTRACT

We present the H I eXtreme (HIX) galaxy survey targeting some of the most H I rich galaxies in the southern hemisphere. The 13 HIX galaxies have been selected to host the most massive H I discs at a given stellar luminosity. We compare these galaxies to a control sample of average galaxies detected in the H I Parkes All Sky Survey (HIPASS, Barnes et al. 2001). As the control sample is matched in stellar luminosity, we find that the stellar properties of HIX galaxies are similar to the control sample. Furthermore, the specific star formation rate and optical morphology do not differ between HIX and control galaxies. We find, however, the HIX galaxies to be less efficient in forming stars. For the most H I massive galaxy in our sample (ESO075-G006, log M_{HI} $[M_\odot]$ = (10.8 ± 0.1)) the kinematic properties are the reason for inefficient star formation and H I excess. Examining the Australian Telescope Compact Array (ATCA) H I imaging and Wide Field Spectrograph (WiFeS) optical spectra of ESO075-G006 reveals an undisturbed galaxy without evidence for recent major, violent accretion events. A tilted-ring fit to the H I disc together with the gas–phase oxygen abundance distribution supports the scenario that gas has been constantly accreted onto ESO075-G006 but the high specific angular momentum makes ESO075-G006 very inefficient in forming stars. Thus a massive H I disc has been built up.

Key words: galaxies – individual: ESO075-G006, galaxies – kinematics and dynamics, galaxies – ISM

1 INTRODUCTION

Over the last two decades large, systematic surveys of the atomic hydrogen (H I) content of galaxies have allowed us to study the relation between star formation, stellar and H I content of galaxies. Scaling relations have shown that the H I content of galaxies in the local universe is well correlated with the galaxies' stellar content (Haynes et al. 1984; Catinella et al. 2010; Dénes et al. 2014; Brown et al. 2015). For this work, outliers towards the very H I rich end of such scaling relations are examined aiming to investigate why these galaxies host a more massive H I disc than average. Two scenarios are considered: these galaxies are either more efficient at accreting gas from their environment, or they are less efficient at converting available gas into stars than H I poor galaxies (see also Huang et al. 2014). A combination of the two scenarios is also possible.

The mechanisms through which galaxies can accrete gas and replenish their gas reservoir are broadly separated into two categories: gas rich mergers ('clumpy accretion') or accretion of gas from the halo or the intergalactic medium ('smooth accretion').

Gas-rich mergers may include both minor and major mergers. Major mergers have been found to be a less domi-

⋆ E-mail: klutz@swin.edu.au

© 2016 The Authors

nant channel of gas accretion both in observational work and simulations (e. g. van de Voort et al. 2011, Wang et al. 2013 and also Sancisi et al. 2008; Sánchez Almeida et al. 2014 and references therein). A series of gas-rich minor mergers may contribute to the gas replenishment of galaxies but observations have shown that also this channel does not deliver enough gas to a galaxy to sustain star formation (Di Teodoro & Fraternali 2014).

In the local universe indirect evidence of cosmological gas accretion has been found: the integrated metallicity of galaxies is lower than expected in chemical evolution models of a closed and isolated galaxy (van den Bergh 1962, Sánchez Almeida et al. 2014 and references therein). Hence, the gas content of a galaxy needs to be replenished with metal-poor gas, i. e. gas originating from the intergalactic medium. This is supported by cosmological hydrodynamical simulations by Davé et al. (2013), who among others have shown that the cycle of gas inflow, gas outflow and star formation is essential to reproduce scaling relations between two or three properties of galaxies, such as the gas content, the stellar content, the star formation activity or the metallicity. In particular the stellar mass-metallicity relation (Hughes et al. 2013; Mannucci et al. 2010) is driven by smooth, stochastic accretion: the accretion of cosmological gas triggers star formation (increase of star formation) and dilutes the interstellar medium (decrease of the gas phase metallicity). Furthermore, Moran et al. (2012) find that massive galaxies with a higher H I content have a steeper drop in gas-phase oxygen abundance. Putting this in the context of cosmological gas accretion, it implies that the outskirts of a galaxy are diluted by metal-poor inflowing gas. It is, however, suggested that in the local universe cosmological accretion is less efficient than at higher redshifts, as the HALOGAS survey was not able to detect the necessary amount of H I clouds to sustain star formation (Heald et al. 2011; Heald 2015).

In addition to cosmological gas accretion the 'Galactic Fountain' mechanism can facilitate the accretion of hot halo gas onto the galaxy (Fraternali et al. 2011; Oosterloo et al. 2007). In this model, the supernova driven galactic fountain initially expels metal-rich gas from the galactic disc into the halo. This now extra-planar gas cools down and falls back onto the disc. As this happens hot halo gas condenses onto the expelled gas, cools and gets dragged along into the disc. Thus, the gas content of the disc increases (Marinacci et al. 2010, 2011). In H I observations the expelled, extra-planar gas can be identified by its lag in rotation velocity. An example for this process could be NGC 891 (Fraternali et al. 2011; Oosterloo et al. 2007), but also several galaxies observed in the context of the HALOGAS survey (Heald et al. 2011; Gentile et al. 2013) have shown evidence for lagging extra-planar gas. It is to be noted though that evidence for sufficient density of hot haloes is scarce (see e. g. Bogdán et al. 2015).

The alternative is that these very gas rich galaxies are inefficient at converting their available gas into stars. Wong et al. (2016) suggest that the H I based star formation efficiency (SFE) is in particular related to the stability of a disc. An elevated specific angular momentum can be one mechanism to stabilise a disc towards gravitational instabilities (Krumholz & Burkhart 2016; Forbes et al. 2014) and we therefore consider it as a reason for decreased SFE. An enhanced angular momentum has two effects on the galaxy. One is keeping recently accreted gas at larger galactocentric radii and lower densities (Kim & Lee 2013; Forbes et al. 2014), where conditions are less favourable for star formation. Secondly, a high angular momentum stabilises the gas against Jeans instabilities and subsequent star formation (Toomre 1964; Obreschkow et al. 2016). Simulations suggest that the angular momentum in a local galaxy is independent of the angular momentum of the host halo (Stevens et al. 2016b), but is determined by the merger history and feedback (Genel et al. 2015; Lagos et al. 2016). Furthermore, the angular momentum is thought to constrain the upper envelope of the gas fraction - stellar mass plane (Maddox et al. 2015).

In this paper we present the H I eXtreme (HIX) galaxy survey. For this survey we are targeting galaxies that contain at least 2.5 times more H I than expected from their stellar luminosity. In order for these galaxies to accumulate that much H I we expect them to have either gone through a recent episode of elevated gas accretion (both smooth and clumpy), to be unable to form stars efficiently from their gas reservoir or a combination of these two scenarios.

The HIX and a control sample of galaxies are observed in H I with the Australian Telescope Compact Array (ATCA) and optical integral field spectra are obtained with the WIFES spectrograph for the HIX galaxies. This combined data set plus publicly available data allow to search for evidence of gas accretion as well as inefficient star formation as a reason for the H I excess.

The term H I excess has been used in many different ways. We use the term "H I excess" to describe a more massive H I content than expected from optical properties.

This article is structured as follow. In section 2, we outline the sample selection and the survey strategy. In section 3, we present observed and publicly available data as well as the data reduction. Section 4 compares our sample to the broader galaxy population. Section 5 focuses on the most extreme galaxy in our sample, ESO075-G006, and in sections 6 and 7 we discuss our findings and conclude.

Throughout the paper we will assume a flat ΛCDM cosmology with the following cosmological parameters: $H_0 = 70.0\,\mathrm{km\,Mpc^{-1}\,s^{-1}}$, $\Omega_m = 0.3$. All velocities are used in the optical convention (cz).

2 SURVEY DESCRIPTION AND SAMPLE SELECTION

2.1 Sample selection

The sample of HIX galaxies is selected from a parent sample of 1796 galaxies in the Southern hemisphere. This is a subset of the HIPASS catalogue and the HIPASS bright galaxy catalogue (Meyer et al. 2004; Koribalski et al. 2004) including only H I detections with reliable, single optical counterparts. This sample has been compiled by Dénes et al. (2014) to obtain scaling relations between the stellar and the H I content of galaxies. Using their scaling relation between the *R*-band luminosity as published in HOPCAT (Doyle et al. 2005) and the HIPASS H I mass, an H I mass is predicted for each galaxy and compared to the H I mass as measured from the integrated 21 cm emission line in HIPASS.

The detailed selection criteria for the HIX sample are:

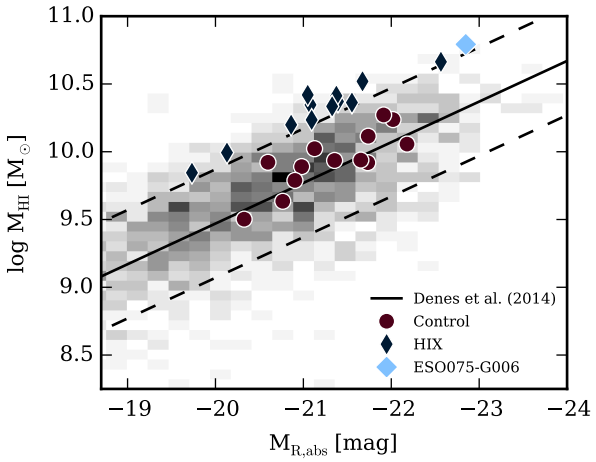

Figure 1. The sample selection: The blue diamonds represent the HIX sample, the red circles the control sample. The light blue, wide diamond marks the data of galaxy ESO075-G006. The grey shade in the background represents the distribution of the HIPASS parent sample. The black solid line gives the Dénes et al. (2014) scaling relation and the black dashed line marks, where the measured H I mass is 2.5 times larger or smaller than the expected H I mass.

(i) an HIPASS measurement of at least 2.5 times more H I than expected from the scaling relation. Figure 1 shows the scaling relation by Dénes et al. (2014) between the *R*-band absolute magnitude and the HIPASS H I mass, which was used here.

(ii) absolute *K*-band magnitude $M_K < -22.0$ mag, restricting the sample to massive spiral galaxies. This is equivalent to a *K*-band luminosity $\log L_K[L_\odot] = 42.8$ or a stellar mass of $\log M_\star[M_\odot] = 9.7$.

(iii) declination < -30 deg for observability with the Australian Telescope Compact Array (ATCA).

We furthermore exclude galaxies near the galactic plane where the high density of foreground stars complicates the photometric measurements.

SuperCOSMOS B-band images (Hambly et al. 2001a,b) and NED[1] have been searched for neighbouring galaxies within the size of the HIPASS spatial resolution element of 15.5 arcmin (Barnes et al. 2001). As no galaxies of similar angular size and brightness have been found, H I-excess due to source confusion can be excluded. Some galaxies, however, are accompanied by small dwarf galaxies. Basic properties of the H I-excess galaxies are given in Table 1.

The parent sample for the HIX galaxies is a subset of HIPASS. It is therefore already an H I selected sample which is biased towards H I rich systems. Selecting the outliers from this parent sample leads to the HIX galaxies being the most extreme galaxies with regards to their (relative) H I mass in the Southern hemisphere.

2.2 Control and comparison samples

In order to compare the HIX sample to a sample of average HIPASS galaxies, a control sample has been compiled. The control galaxies were drawn from the same parent sample and the selection criteria (ii) and (iii) were the same as used to define the HIX sample. However, criterion (i) was changed to:

(i) a measured HIPASS H I mass between 1.6 times less and more than what is expected from the scaling relation in order to capture galaxies well within the scatter (0.3 dex).

The ATCA Online Archive[2] (ATOA) was searched for observations of those galaxies that follow the control sample selection criteria. This lead to 13 control galaxies, that have been observed for at least one synthesis in any 1.5-km array configuration of ATCA. In Figure 1 these galaxies are drawn as red circles and lie well within the scatter of the scaling relation. More details and basic properties of the control sample are given in Table 1.

It is to be noted that the control sample is selected to be normal for an H I selected sample as e. g. HIPASS. This implies that the control sample is potentially still H I rich compared to a stellar mass selected sample.

3 OBSERVATIONS, DATA REDUCTION AND AUXILIARY DATA

3.1 ATCA observations

In this work we only present the ATCA observations for ESO075-G006, which is the most extreme galaxy in our sample with respect to (relative) H I mass and will be further discussed in Section 5. The ATCA H I data of the remaining HIX and control galaxies will be presented in a subsequent paper.

For the observations of ESO075-G006, the standard ATCA flux and bandpass calibrator PKS 1934-638 has also been observed as the phase calibrator, which was visited regularly during the observations. The observations were carried out between November 2012 and January 2013. On source times are 5.6 h, 9.3 h and 5.6 h in the 1.5D, 750C and EW367 array configurations respectively. The Compact Array Broadband Back end (CABB, Wilson et al. 2011) allows to observe continuum and spectral line simultaneously. The continuum band is 2048 MHz wide, has a frequency resolution of 1 MHz and is centred on 2.1 GHz. Spectral line observations cover a 8.5 MHz bandwidth with a channel width of 0.5 kHz. This is equivalent to a velocity resolution of 0.1 km s^{-1} at 1370 MHz, which is the band's central frequency. In this paper we only utilise the spectral line data, which will be smoothed to channel widths of 4 and 10 km s^{-1}.

3.2 Radio data reduction and analysis

The data reduction of the ATCA H I observations is completed using standard tasks in the program package MIRIAD (Sault et al. 1995) and the python wrapper MIRPY[3].

After removing radio frequency interference, a semi-automated pipeline conducts bandpass, flux and, phase calibration and subtracts a first order polynomial baseline for

[1] http://ned.ipac.caltech.edu/

[2] http://atoa.atnf.csiro.au/

[3] https://pypi.python.org/pypi/mirpy

ID (1)	RA (2)	DEC (3)	log $M_\star$[$M_\odot$] (4)	log M_{HI}[$M_\odot$] (5)	log $M_{HI}/M_\star$ (6)	V_{sys} [km s^{-1}] (7)	D [Mpc] (8)	log SFR [$M_\odot\,yr^{-1}$] (9)
HIX								
ESO111-G014	00:08:18.8	-59:30:56	10.5	10.6	0.093	7786	112	0.33
ESO243-G002	00:49:34.5	-46:52:28	10.5	10.5	–0.014	8885	129	0.16
NGC 0289	00:52:42.4	-31:12:21	10.4	10.3	–0.049	1629	23	0.081
ESO245-G010	01:56:44.5	-43:58:21	10.4	10.3	–0.075	5740	82	0.27
ESO417-G018	03:07:13.2	-31:24:03	10.2	10.4	0.14	4746	67	0.18
ESO055-G013	04:11:43.0	-70:13:59	10.1	10.4	0.25	7386	105	0.21
ESO208-G026	07:35:21.1	-50:02:35	9.79	9.89	0.090	2983	40	-0.50
ESO378-G003	11:28:04.0	-36:32:34	9.96	10.2	0.20	3021	41	-0.24
ESO381-G005	12:40:32.7	-36:58:05	10.2	10.4	0.21	5695	80	0.22
IC 4857	19:28:39.2	-58:46:04	10.4	10.0	–0.33	4679	67	0.37
ESO461-G010	19:54:04.4	-30:29:03	10.0	10.4	0.40	6709	98	-0.13
ESO075-G006	21:23:29.5	-69:41:05	10.5	10.8	0.29	10609	154	0.46
ESO290-G035	23:01:32.5	-46:38:47	10.4	10.3	–0.11	5881	84	0.012
CONTROL								
NGC 0685	01:47:42.8	-52:45:42	9.81	9.53	–0.28	1362	18	-0.63
ESO121-G026	06:21:38.8	-59:44:24	10.4	9.95	–0.46	2268	30	0.12
ESO123-G023	07:44:38.9	-58:09:13	10.1	10.0	–0.06	2914	39	-0.54
NGC 3001	09:46:18.7	-30:26:15	10.8	10.0	–0.81	2464	32	0.39
ESO263-G015	10:12:19.9	-47:17:42	10.3	9.67	–0.67	2531	33	-0.27
NGC 3261	10:29:01.5	-44:39:24	10.8	10.1	–0.76	2564	34	0.26
NGC 4672	12:46:15.7	-41:42:21	10.7	10.3	–0.43	3273	45	0.30
NGC 5161	13:29:13.9	-33:10:26	10.5	10.1	–0.34	2390	32	0.14
ESO383-G005	13:29:23.6	-34:16:17	10.4	9.75	–0.67	3614	50	-0.18
IC 4366	14:05:11.5	-33:45:36	10.7	10.1	–0.61	4615	65	0.54
ESO462-G016	20:23:39.0	-28:16:40	10.1	9.85	–0.23	3055	45	0.073
ESO287-G013	21:23:13.9	-45:46:23	10.5	10.2	–0.34	2697	39	0.18
ESO240-G011	23:37:49.9	-47:43:41	10.9	10.3	–0.55	2840	40	-0.0013

Table 1. The H I extreme and control galaxy sample. *Column* (1): An ID for every galaxy. *Column* (2) and (3): RA and DEC taken from 2MASS. *Column* (4): The stellar mass calculated as described in Section 3.6. *Column* (5): The H I mass calculated following Equation 1 using the measured HIPASS flux and the distance as stated in *Column* (8). *Column* (6): The H I gas mass fraction is defined as $f_{HI} = \frac{M_{HI}}{M_\star}$. *Column* (7): The heliocentric, systemic velocity from HIPASS (Meyer et al. 2004). Velocities here and throughout the paper are given in the optical convention (cz). *Column* (8): Luminosity distance calculated from the systemic velocity in column 7 converted to the Galactic Standard of Rest frame and assuming our standard cosmology. *Column* (9): The star formation rate measured as described in Section 3.6.

each array configuration separately. All available observations from different array configurations are then combined in the Fourier transformation. For the detailed analysis of the H I properties of ESO075-G006 in Section 5, two different data cubes were produced. The cube for the moment analysis has been combined by using a Brigg's robust parameter of 0.5 and a channel width of 4 km s^{-1} to maximise sensitivity, the cube for the tilted ring fit with a robust parameter of 0.0 and a velocity channel width of 10 km s^{-1} to maximise spatial resolution. As the longest baselines with Antenna 6 are in most cases too long to pick up signal from diffuse and extended H I and merely add noise to the data, all baselines with Antenna 6 are excluded. For the H I data of ESO075-G006, this leads to synthesised beam sizes of 52.4 arcsec by 41.2 arcsec (rob=0.5) and 40.6 arcsec by 25.3 arcsec (rob=0.0) and a noise level of 1.81 mJy $beam^{-1}$ and 1.2 mJy $beam^{-1}$ respectively. The lowest column density limit in the moment analysis (on rob=0.5 data) assumes a $3\,\sigma$ detection over a velocity width of 12 km $s^{-1}$and amounts to 70 mJy $beam^{-1}$ km s^{-1} = $0.4 \cdot 10^{20}$ cm^{-2} = 0.3 $M_\odot$ pc^{-2}. Moment maps have been created with the MIRIAD task *moment*, including a $3\,\sigma$ clipping. Moment 1 and 2 maps are further masked to the lowest column density contour and all moment maps are regridded to the resolution of the SuperCOSMOS optical image.

The resulting ATCA data cubes are then further analysed with standard MIRIAD tasks, SAOImage DS9, TiRiFiC (Józsa et al. 2007) and python scripts [4].

3.3 WiFeS observations

ESO075-G006 has also been observed with the Wide Field Spectrograph (WiFeS, Dopita et al. 2007) integral field unit (IFU) mounted on the Siding Spring Observatory ANU 2.3 m telescope. ESO075-G006 has been observed with three pointings towards the north-western edge, the centre and the south-eastern edge of the disc. WiFeS has been setup with R = 3000 gratings in both the red and blue arm in combination with the dichronic set at 560 nm. For reliable skyline subtraction, galaxy data have been taken in the nod-and-shuffle mode. Every night of observations has been completed with standard calibration images including bias, sky and dome flat field and wire imaging for centring the slitlets as well as NeAr and CuAr arc lamp spectra for wavelength

[4] https://www.python.org/

Pointing (1)	RA (2)	DEC (3)	PA (4)	t_{exp} (5)
Centre	21:23:28.7	-69:41:02	165 °	1800s
South	21:23:30.7	-69:41:31	75 °	3600s
North	21:23:26.9	-69:40:32	75 °	1800s

Table 2. Details for the three WiFeS pointings on ESO075-G006. *Column* (1): an ID for the pointing. *Column* (2) and (3): the central coordinates. *Column* (4): the rotator angle of the spectrograph. *Column* (5): the total on-source exposure time.

calibration. Two to three times a night a standard star for flux calibration has been observed. The observations of ESO075-G006 have been conducted in August 2014, July and October 2015 under photometric conditions. For more details of the three pointings see Table 2.

3.4 WiFeS data reduction and analysis

Childress et al. (2014) provide the fully automated PyWiFeS pipeline for WiFeS data. This pipeline includes bad pixel repair, bias and dark current subtraction, flat fielding, wavelength calibration, sky subtraction, flux calibration and data cube creation. The resulting data cubes are 70 by 25 pixels (35 by 25 arcsec) in size.

PyWiFeS is run on each observed galaxy data cube individually. For each pointing, data cubes are median stacked afterwards. This way small spatial offsets between observations can be taken into account. This procedure results in two data cubes for each pointing: one containing the red half of the spectrum and the other one the blue half.

One stellar population model is constructed for each pointing by median stacking the spectra of all spaxels in one pointing. The stellar population fit is conducted on both the red and blue cube together using the pPXF method and complimentary Python script by Cappellari & Emsellem (2004). The stellar population model library is taken from Vazdekis et al. (2010).

For the measurement of the emission line strength the data cubes of the red and blue half of the spectrum are analysed independently. Each individual data cube is Voronoi binned following Cappellari & Copin (2003); Cappellari (2009). The Voronoi binning is constructed such that the signal to noise ratio in the wavelength range around the O[III] (blue) or N[II] line (red) reaches 50. The error map necessary for the binning is constructed from the variance data cube as given by the PyWiFeS pipeline. The size of final Voronoi bins are between 1 and 200 spaxels. In each Voronoi bin the stellar continuum model as fitted to the entire pointing is subtracted. Emission lines are fitted with Gaussians in each Voronoi bin. This results in a redshift measurement from the Hα line and line strengths that can be used to estimate the gas-phase oxygen abundance.

The Voronoi bins of the red and the blue arm are different. So each pixel is assigned the value of the entire bin and metallicities are calculated on a pixel by pixel basis.

3.5 Public Data

In addition to the observed data, publicly available data are also used:

(i) The HIPASS survey data are used to calculate the H I mass (Barnes et al. 2001; Meyer et al. 2004; Zwaan et al. 2004).

(ii) The AllWISE data release (Cutri et al. 2013) of the *WISE* mission (Wright et al. 2010) provides imaging in the four mid-infrared *WISE* bands: W1 (3.4 μm), W2 (4.6 μm), W3 (12 μm), W4 (22 μm). The flux of galaxies in each band is measured from images obtained from the ICORE co-adder[5] (Masci & Fowler 2009) and converted into magnitudes following the prescription in Cutri et al. (2013).

(iii) The catalogue of extended sources in the Two Micron All Sky Survey (2MASX, Skrutskie et al. 2006) provides magnitudes in the J, H and K-band and precise coordinates of the centre of the stellar disc.

(iv) The HIPASS optical counter part catalogue (HOPCAT, Doyle et al. 2005) provides B_j, R and I-band magnitudes, optical position angles and optical semi-major to semi-minor axis ratios from SuperCOSMOS (Hambly et al. 2001a,b). HOPCAT also states the Galactic extinction measures $E(B-V)$ at the location of each galaxy as estimated by Schlegel et al. (1998).

(v) Optical imaging used in this work is obtained from the SuperCOSMOS (Hambly et al. 2001a,b) web page[6].

(vi) The ESO-LV catalogue (Lauberts & Valentijn 1989) provides both isophotal diameters and diameters at 90 per cent B light

(vii) Near- and far ultraviolet (NUV, FUV) photometry has been measured from the Galaxy Evolution Explorer imaging (*GALEX*, Martin et al. 2005; Morrissey et al. 2007). *NUV* images are available for all except one HIX galaxy (ESO208-G026) and except four control galaxies (NGC 685, NGC 3001 and NGC 3261, ESO123-G023). *NUV* counts are measured from intensity maps and converted into magnitudes using *GALEX*'s flux calculator [7].

The *WISE* and *GALEX* photometry is remeasured in elliptical apertures, where the semi major axis is of the size of the ESO-LV 25 mag arcsec^{-2} isophotal radius and the axis ratio is taken from HOPCAT. Stars are masked out. The local sky background is estimated from dedicated background apertures and subtracted either with FUNTOOLS[8] (GALEX) or as prescribed in the supplement (WISE).

The 2MASS data for the HIPASS parent sample are retrieved from the VizieR catalogue access tool, which also took care of reliable cross-matching.

3.6 Estimating galaxy properties

The H I mass is calculated from the published HIPASS integrated 21 cm emission signal by:

$$M_{HI}[M_\odot] = \frac{2.356 \cdot 10^5}{1+z} \cdot (D[Mpc])^2 \cdot F_{HI}[Jy\,km\,s^{-1}] \quad (1)$$

with z being the galaxy's redshift, D the distance to the galaxy in Mpc and F_{HI} the integrated flux density in units of Jy km s^{-1}. The error estimation closely follows the error

[5] http://irsa.ipac.caltech.edu/applications/ICORE/
[6] http://www-wfau.roe.ac.uk/sss/index.html
[7] http://asd.gsfc.nasa.gov/archive/galex/FAQ/counts_background.html
[8] https://github.com/ericmandel/funtools

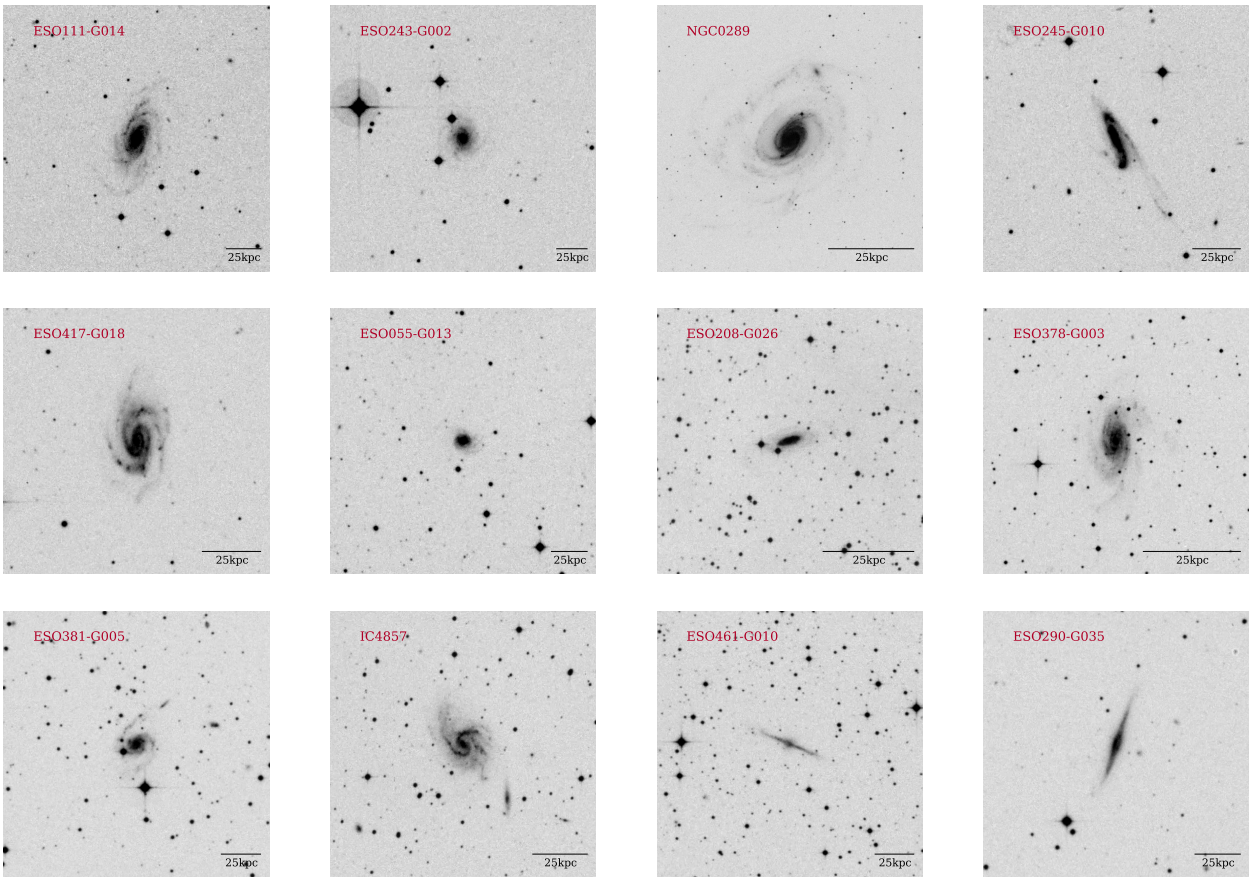

Figure 2. Panel of SuperCOSMOS B_j-band post stamp images of all HIX galaxies. All images are 3 arcmin by 3 arcmin in size except for the image of NGC 289, which is 6 arcmin by 6 arcmin in size. The scale bar in the bottom right corner indicates 25 kpc at the distance of the galaxy. The optical image of ESO075-G006 is shown further down in Section 5.

estimation of F_{HI} as suggested by Koribalski et al. (2004):

$$S/N = \frac{S_{peak}}{\sqrt{rms^2 + (0.05 \cdot S_{peak})^2}} \quad (2)$$

$$\Delta F_{HI} = \frac{4}{S/N} \cdot \sqrt{S_{peak} \cdot F_{HI} \cdot dv} \quad (3)$$

where S_{peak} is the peak intensity in the spectrum, rms the root mean square of the data cube and dv the velocity resolution. Using Gaussian error propagation the error of F_{HI} is then propagated and combined with the error of the distance to estimate the error of the H I mass.

All stellar masses for the HIX, control and HIPASS samples were estimated following equation (3) in Wen et al. (2013), which assumes a linear relationship between the log of the stellar mass and the log of the Galactic extinction corrected 2MASS K-band luminosity.

Baryonic masses for HIX and control sample are the sum of atomic and stellar mass. The atomic gas mass is the H I mass increased by 35 per cent to include Helium.

Star formation rates (SFR) for the HIX, control and HIPASS samples are estimated using the *GALEX NUV* luminosity in combination with the *WISE W3*-band luminosity to account for dust obscured star formation. We use the prescription in equation (1) and (2) in Saintonge et al. (2016) assuming a Chabrier (2003) initial mass function (IMF). Where *GALEX* photometry is not available, the SFR prescription by Cluver et al. (2014), which is based solely on the luminosity in the *W3*-band, is used. Their IMF is consistent with a Chabrier (2003) IMF and the comparison of SFRs estimated with the both methods does not reveal systematic offsets. ESO075-G006 is not detected in the *W3*-band. Its SFR does therefore not include a mid-IR component.

The gas-phase oxygen abundance is estimated with the O3N2 and N2 method using the Hα, Hβ, [O III]λ5007 Å and [N II]λ6584 Å emission lines as described by Pettini & Pagel (2004).

4 THE HIX SAMPLE IN CONTEXT

In this section the HIX galaxy sample is presented and compared to the control sample, the parent sample and other H I rich samples, where appropriate data are available.

As a first overview, Figure 2 shows the optical images of all HIX galaxies except ESO075-G006, for which the optical image is shown Section 5. All HIX galaxies are spiral galaxies. One of them shows clear signs of interaction (ESO245-G010), the remaining galaxies appear quite regular.

4.1 HI mass and stellar mass

The relation between gas fraction (defined as $M_{HI}/M_\star$) and stellar mass is well known and used here to test the HIX selection criteria and compare the HIX galaxies to the control and parent sample as well as other samples.

Figure 3 shows this relation. Most HIX galaxies are located above the $1\,\sigma$ scatter of the parent sample, while the control galaxies populate the HIPASS scatter. The two HIX galaxies that are located within the grey shaded area are ESO208-G026 and IC 4857. They have been selected to be H I excess galaxies according to the *R*-band scaling relation of Dénes et al. (2014). On the gas mass fraction vs. stellar mass plane, however, they lie within the scatter of the HIPASS parent sample and thus, their H I-richness on that scale is not as obvious as for the other HIX galaxies. In a future analysis of spatially resolved H I data of these galaxies, we will determine whether these two galaxies are true HIX galaxies, more "normal" HIPASS galaxies or something in between.

For comparison, Figure 3 also shows the running average of the GASS sample (data release 3, Catinella et al. 2010, 2012, 2013). Non-detections are included as upper limits. GASS is a stellar mass selected sample and as such not biased towards H I rich systems as it is the case for HIPASS. The running average of the GASS sample is therefore lower than for the HIPASS parent sample and even our control sample appears H I rich compared to GASS. This further emphasises that the HIX galaxies are among the most H I rich galaxies in the local universe.

We further compare the HIX sample to other surveys of H I rich galaxies: HIghMass (Huang et al. 2014), a sample by Lemonias et al. (2014), H I-Monsters (Lee et al. 2014), HIGHz (Catinella & Cortese 2015) and BLUEDISK (Wang et al. 2013). For HIghMass and Lemonias et al. (2014) sample galaxies, SFRs and stellar masses were calculated the same way as for the HIX galaxies. For the HIGHz and BLUEDISK galaxies those values were taken from the respective publications. For all samples, distances and H I masses were adopted from the respective publications.

HIghMass and Lemonias et al. (2014) galaxies have been selected from ALFALFA (Giovanelli et al. 2005) using the $\log f_{HI}$ - $\log M_\star[M_\odot]$ scaling relation. Thus, both samples are also located above the $1\,\sigma$ scatter of HIPASS. While the Lemonias et al. (2014) sample focusses on early type, AGN hosting galaxies, HIghMass galaxies are spirals. HI-Monsters are HI massive galaxies ($\log M_{HI}[M_\odot] > 10.3$) from ALFALFA, i.e. very similar to HIghMass. The HI-Monsters sample includes in addition a selection of low surface brightness (LSB) galaxies like Malin 1. HIGHz are a sample of the highest redshift HI detections of single galaxies. The BLUEDISK sample has been selected to be H I rich for their morphology and star formation activity. Figure 3 shows that these BLUEDISK galaxies lie well within the $1\,\sigma$ scatter of HIPASS.

In being H I massive and spiral galaxies, the HIghMass (and H I-Monsters) sample galaxies appear to be the most similar to the HIX sample.

As none of the HIX galaxies is a LSB galaxy and most of the H I-Monsters have larger stellar masses than the HIX galaxies, there is little overlap between these studies. Where both samples overlap, they host comparably massive H I reservoirs at a given stellar mass.

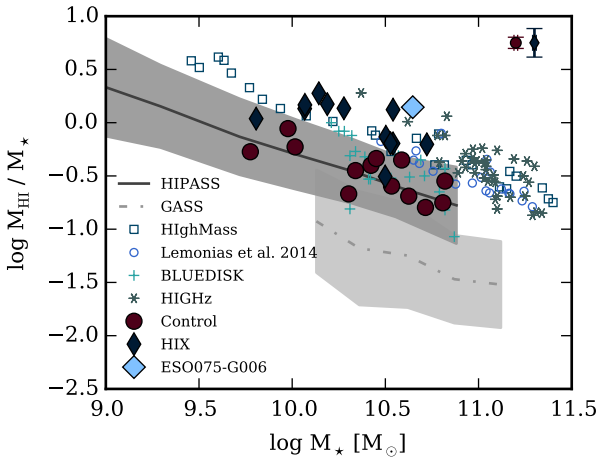

Figure 3. The H I gas mass fraction as a function of the stellar mass. The blue diamonds present the HIX sample and red circles the control sample. The light blue diamond is ESO075-G006, which will be discussed in more detail further below. Blue and red errorbars in the top right corner give the median errorbars for the HIX and control sample respectively. The dark grey, solid line presents the running average of the HIPASS parent sample along with the $1\,\sigma$ scatter as the grey shaded region. The light grey, dashed line and shaded area represents the running average and $1\,\sigma$ scatter of the GASS sample. Open symbols present other surveys of (H I rich) galaxies: HIghMass (squares), Lemonias et al. (2014) (circles), HIGHz (asterisks) and BLUEDISK (crosses).

Similar to the HIX survey, the HIghMass survey aims to select the most H I extreme galaxies from an H I selected survey (in this case from ALFALFA). To compare the two sample selections, we use the 2MASS stellar masses for our HIPASS parent sample. These are only available for 1475 out of 1796 galaxies. We further cut this sample down to galaxies, that (a) are located at dec< −30 deg, (b) are more massive than our stellar mass cut ($M_K < -22.0$ mag) and (c) are neither in close proximity to the Galactic plane (for good photometry) nor a massive neighbouring galaxy (exclude source confusion). Applying the HIghMass sample selection to this parent sample yields 22 galaxies. These 22 galaxies include all HIX galaxies except for the two galaxies that are also located in the HIPASS $1\,\sigma$ scatter in Figure 3 (ESO208-G026, IC 4857). The remaining 11 galaxies in this "HIPASS-HIghMass" sample do not appear in the HIX survey because they are not outliers to the Dénes et al. (2014) scaling relation. This means, when estimating their H I mass from their *R*-band luminosity, the estimated H I mass is not 2.5 times larger than their measured H I mass. Three of the HIghMass like galaxies that are not in HIX have large stellar masses ($\log M_\star[M_\odot] \approx 11.0$). There are, however, no differences found, when comparing the distribution of H I mass and H I mass fraction of the HIX like galaxies and HIghMass like galaxies above our stellar mass cut.

4.2 Star formation activity

In order to further characterise the sample of HIX galaxies, we investigate their star formation activity and compare it to the control sample.

In Figure 4, the scatter plot shows the relation between

the star formation efficiency (SFE) defined as SFR divided by H I mass, and stellar mass for the HIX and control samples. This definition has been used before by e. g. Wong et al. (2016) and Schiminovich et al. (2010). We obtain a linear fits to the data with a Monte Carlo method. This method includes creating 1000 random samples that have the same mean and standard deviation in stellar mass and SFE as the sample, to which the line is fitted. To each of these random samples, a line is then fitted with a standard least squares fit. The final slope and interception of the fit is then mean of the results of the 1000 random samples.

The average specific star formation rates of HIX ($\log \mathrm{sSFR}[\mathrm{yr}^{-1}] = (-10.3 \pm 0.2)$) and control sample ($\log \mathrm{sSFR}[\mathrm{yr}^{-1}] = (-10.4 \pm 0.2)$) are comparable, i. e. at a given stellar mass both samples form stars at a similar rate. However, as HIX galaxies are more H I rich than the control sample, their SFE are systematically lower as can be seen in Figure 4.

IC 4857 is the only HIX galaxy that forms stars at similar efficiency as the control sample. ESO123-G023 and ESO240-G011 are the least efficient control galaxies.

The model by Wong et al. (2016) is calibrated on SINGG galaxies (HI selected, Meurer et al. 2006) and comes in two flavours: The relative contributions by H I and H_2 are disentangled using a prescription either dependent on the stellar surface mass density (D) or the hydrostatic pressure (P). While the hydrostatic pressure model is the preferred model by Wong et al. (2016), the stellar surface mass density model better describes the SFEs of the control sample. The HIX galaxies form stars less efficiently than suggested by both models. All galaxies form stars less efficiently than the average value found by Schiminovich et al. (2010). It is to be noted though that the scatter of their data is three orders of magnitudes. The SFEs of all HIX and control galaxies are larger than $10^{-10.75}\,\mathrm{yr}^{-1}$. Below this SFE, Schiminovich et al. (2010) consider a galaxy passive for their H I reservoir.

Linear fits to the SFEs of the HighMass and Lemonias et al. (2014) galaxies are also shown in Figure 4. In particular the linear fit to the HighMass galaxies is very close to that of the HIX sample further emphasising the similarity of the two samples. Lemonias et al. (2014) galaxies tend to be less efficient than the HIX galaxies. The HIGHz sample is the most efficient at forming stars from their massive H I reservoirs.

To summarise, HIX galaxies form stars less efficiently than the control sample. As outlined in the introduction, one reason for decreased SFE can be the increased angular momentum of a galaxy. In the following section we will discuss ESO075-G006, for which the resolved ATCA H I data will be analysed and the increased angular momentum hypothesis will be tested.

5 THE MOST EXTREME: ESO075-G006

ESO075-G006 hosts the most massive H I disc of the HIX galaxies with an H I mass of $\log \mathrm{M_{HI}}\,[\mathrm{M_\odot}] = (10.8 \pm 0.1)$ as measured in HIPASS. This measured H I mass is 2.6 times larger than expected from its HOPCAT R-band magnitude. An H I mass of almost $10^{11}\,\mathrm{M_\odot}$ is rare. According to the H I mass function by Martin et al. (2010) based on ALFALFA, in a volume of 400,000 Mpc^3 one expects to find only one galaxy to hosts an as massive H I disc as ESO075-G006.

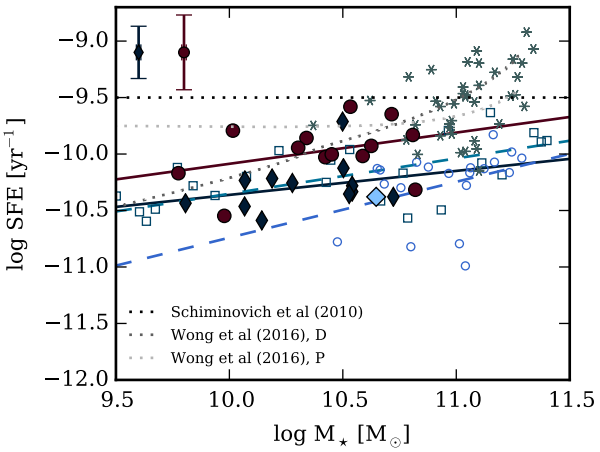

Figure 4. The star formation efficiency as a function of stellar mass. Symbols are as in Figure 3. The red, solid line is a fit to the HIX data and the blue, solid line a fit to the control data. The black, dotted line is the average SFE for $\log \mathrm{M_\star/M_\odot} > 10$ galaxies found by Schiminovich et al. (2010) and the grey, dotted lines are model predictions by Wong et al. (2016). For comparison, the light blue, dashed lines are fits to the HighMass and Lemonias et al. (2014) samples respectively (colours as for their symbols).

In this section the optical morphology, the H I properties and kinematics, the optical spectra and the local environment of ESO075-G006 will be discussed. This section aims to understand the reason for the H I excess in the most extreme HIX sample galaxy. Similar analysis for the remaining HIX galaxies and a comparison to the control sample will be presented in a future paper.

5.1 Optical morphology of ESO075-G006

The SuperCOSMOS B_j-band image of ESO075-G006 is shown in panel (a) of Figure 6. ESO075-G006 hosts a bar and seems to be accompanied by a dwarf galaxy located to the north-west. In the optical an inner ring and an outer pseudo ring is visible as the RC3 morphological classification indicates. The inner ring is also visible in *GALEX NUV* images as a star forming ring (see grey scale image in Figure 10, exposure time: 207 s). As both the SuperCOSMOS and *GALEX NUV* imaging is relatively shallow, faint spiral arms or an XUV disc can not be excluded. There is no *GALEX FUV* image available. The stellar mass is calculated as $\log \mathrm{M_\star[M_\odot]} = 10.5$ and the ESO-LV catalogue gives a 25 mag arcsec^{-2} isophotal radius of 30.2 arcsec = 21.7 kpc.

As some of the most H I massive galaxies known, e. g. Malin 1 (Pickering et al. 1997), are low surface brightness (LSB) galaxies, ESO075-G006 is a good candidate for a LSB galaxy. However, when using the central K-band surface brightness as indicator (Monnier Ragaigne et al. 2003), the value of 17.41 mag arcsec^{-2} of ESO075-G006 is brighter than the threshold to LSB discs.

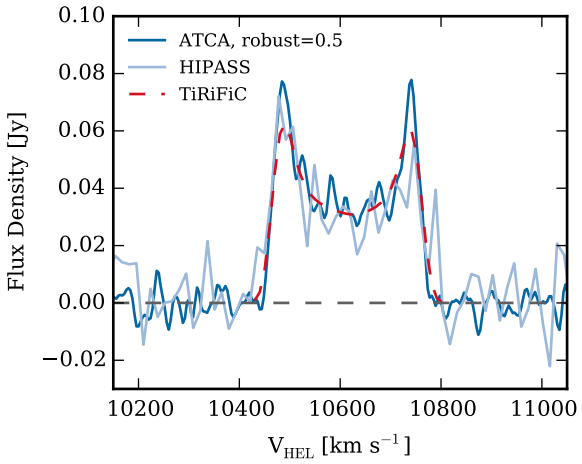

Figure 5. Comparison of H I spectra as measured from the HIPASS data cube (light blue), the ATCA data cubes (dark blue for robust=0 and medium blue for robust=0.5) and the TiRiFiC model data cube (red dashed line, see Section 5.3.2).

5.2 HI morphology and radial column density profiles

The two H I data cubes for ESO075-G006 have been produced as explained in Section 3. In this section we use the robust=0.5, dv=4 km s^{-1} data cube to analyse the distribution of H I in ESO075-G006.

Figure 5 shows the spectrum as taken from the ATCA data cube and from the HIPASS data. They agree within the noise level. The double horn is close to symmetric indicating that the approaching a receding half of the disc contain approximately the same amount of gas. The integrated flux density of ESO075-G006 measured from the ATCA data amounts to 12.8 Jy km s^{-1}. Using Equation 1 this translates into log $M_{HI}[M_\odot] = 10.8 \pm 0.1$, which is in agreement with the HIPASS measurement of log $M_{HI}[M_\odot] = 10.8 \pm 0.2$ and indicates that the ATCA data cube is not missing any diffuse H I.

The H I column density contours overlaid on the optical SuperCOSMOS image are shown in Figure 6 (c). The locations of maximum column density in the H I disc are found to the north and south of the centre and align with the ridge of the central bar. Furthermore, they coincide with the outermost spiral arms as visible in *NUV* and faintly visible in the optical. The approaching and receding half appear very similar, i. e. the disc is symmetric. No obvious signs of interaction and tails are visible. In the centre of the disc the H I column density drops to approximately 1 $M_\odot$ pc^{-2}. This is a common feature of H I discs and hints to molecular gas in the centre of ESO075-G006 (Bigiel & Blitz 2012). The distance between the geometrical centre of the H I disc and the 2MASX coordinates of the stellar disc centre is less than 10 arcsec, which is smaller than the spatial resolution element. Therefore, both coincide. In conclusion, the H I morphology points towards a well settled disc.

Radial profiles of the H I column density are obtained from the moment 0 map by measuring the median column density in co-centric elliptical annuli. In Figure 7 (a) an azimuthally averaged profile is shown. To account for possible disc asymmetries, the annuli were also divided in four quadrants with opening angles of 90 deg centred on either a semi-major or semi-minor axis. This allows for profiles along the semi-major axis in north-western and south-eastern direction. The two profiles along the major axis are also presented in Figure 7 (a). Within the errors of the measurements, the approaching and receding sides show the same radial column density behaviour, again pointing towards a regular H I disc.

The size of an H I disc is commonly quantified through R_{HI}, which is the radius at which the column density of the H I drops to 1 $M_\odot$ pc^{-2}. Broeils & Rhee (1997) and later Wang et al. (2014, 2016) have found R_{HI} to correlate remarkably well with the H I mass of the disc. This relation indicates that the average H I column density in settled H I discs is constant from galaxy to galaxy. For ESO075-G006 $R_{HI} = (74 \pm 4)$ kpc is measured from the azimuthally averaged radial profile in Figure 7 (a) and corrected for beam smearing following Wang et al. (2014, 2016). The measured value is then compared to the expected $R_{HI,exp}$ that is calculated from equation (2) in Wang et al. (2014, 2016). We find $R_{HI,exp} = (74 \pm 18)$ kpc. The measured and expected value are in agreement within the errors. Hence, the average H I column density of ESO075-G006 is normal.

5.3 HI kinematics

In this section we investigate the H I kinematics in detail searching for evidence of recent gas accretion e. g. radial motions or vertical gradients indicating a galactic fountain.

5.3.1 2D moment analysis

Panel (b) of Figure 6 shows the velocity field of ESO075-G006. The iso-velocity contours show the typical spider-web pattern of regularly rotating discs. Radial motions can induce S-shaped iso-velocity contours in the central parts of the galaxy. This, however, is not seen and is a first indication that radial motion are not playing a major role in the velocity field of ESO075-G006.

Figure 6 (d) shows the velocity dispersion of the H I disc of ESO075-G006. The low velocity dispersion in the outer parts, especially along the major axis of the disc further indicates a regularly rotating disc. The increase of the measured velocity dispersion towards the centre of the disc is due to projection effects.

5.3.2 3D kinematic analysis

To further explore the kinematic properties of ESO075-G006, a tilted ring model is fitted to the robust=0, dv=10 km s^{-1} H I data cube using TiRiFiC (Józsa et al. 2007). For the fit 7 rings, each 30 arcsec wide, are defined. In addition two half discs are defined, each centred on the major axis with an opening angle of 180 degrees. This way the approaching and the receding side of the H I disc can be fitted independently. However, only the surface brightness is allowed to vary between the half discs, all other quantities are fitted to full rings. A variety of models were fitted to the data:

(i) a flat rotating disc.
(ii) a warped disc with purely rotational motions.

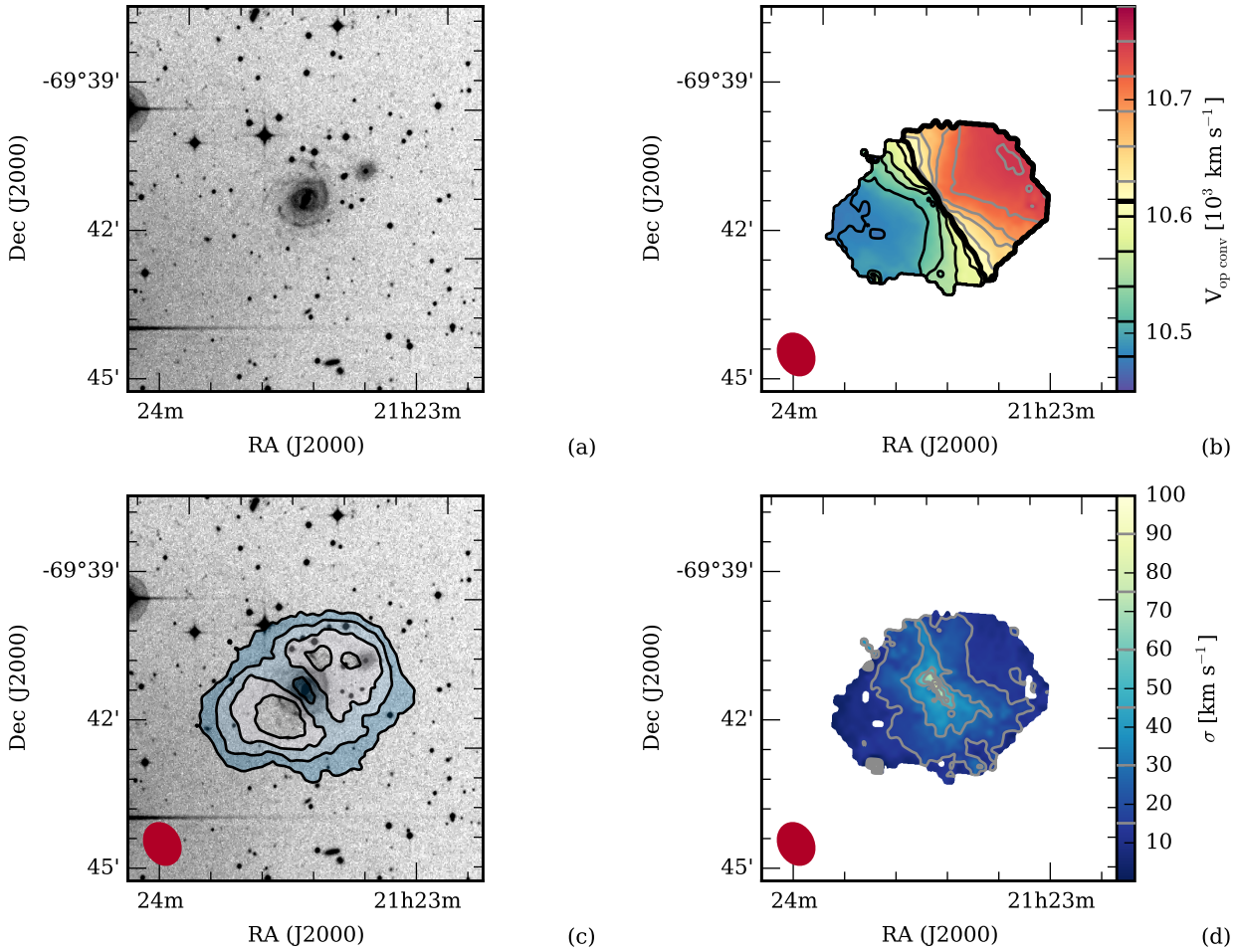

Figure 6. (a) The optical SuperCOSMOS B_j-band image of ESO075-G006. **(b)** The velocity field (moment 1 map) of ESO075-G006 solid and dashed contours are separated by 20 km s^{-1}and indicate the receding and approaching side respectively. The thick black contour is drawn at 10613 km s^{-1}indicating the systemic velocity. **(c)** The column density (moment 0) map of ESO075-G006 overlaid on the SuperCOSMOS optical B-band image. H I column density contours are at (0.3, 1.3, 2.3, 3.3) $M_\odot$ pc^{-2}. **(d)** The velocity dispersion (moment 2) map of ESO075-G006. Contours are separated by 15 km s^{-1}. The red ellipses in the bottom left corners of the moment maps indicate the synthesised beam size. All moment maps are created from the rob=0.5 cube.

(iii) discs with lagging thick discs, i. e. Galactic Fountain mechanism.

(iv) flat and warped discs with radially constant or varying radial velocity components.

(v) rotating discs with a combination of radial velocity components and vertical velocity gradients.

All models return similar values for surface brightness, systemic and rotation velocity, inclination (range), position angle (range) and kinematic centre. The flat disc model is not able to produce a flat rotation curve at large radii but requires a sharp drop in the rotation velocity by 30 km s^{-1}. This model is therefore excluded. More complicated and exotic models (models (iii), (iv) and (v)) do not trace emission in channel maps and position–velocity diagrams better than a warped disc with purely rotational motions. The data are limited by sensitivity and spatial resolution. The effects investigated in models (iii), (iv) and (v) can still occur in ESO075-G006 but we are not able to detect evidence in favour of them. We apply Occam's Razor and select the simplest model with a flat rotation curve, which is the warped disc. In the following, this model is presented and discussed.

The rotation curve is shown in Figure 7 (b). Fitting a rotation curve of the functional form:

$$v_{rot}(r) = v_{flat} \cdot \left[1 - \exp\left(\frac{-r}{l_{flat}}\right)\right] \quad (4)$$

(Leroy et al. 2008 and references therein) yields a rotation velocity of $v_{flat} = (201 \pm 6)$ km s^{-1}.

The model suggests a warp in inclination, which is dropping from 41 to 36 deg between radii of 90 and 120 arcsec. The radial variation of inclination, i. e. the warp is shown in Figure 7 (c). This is a warp at the lower end of the warp scale found e. g. in the THINGS galaxies (Schmidt et al. 2016). The position angle is held constant with radius and is fit to 306 deg (see again Figure 7 (c)).

Furthermore, TiRiFiC finds a velocity dispersion σ of 11.2 km s^{-1}and a systemic velocity of 10613 km s^{-1}. The kinematic centre of the disc is located at 21h 23′ 29.5″ −69° 41′ 06″, which is the same location as the 2MASX centre of the stellar disc.

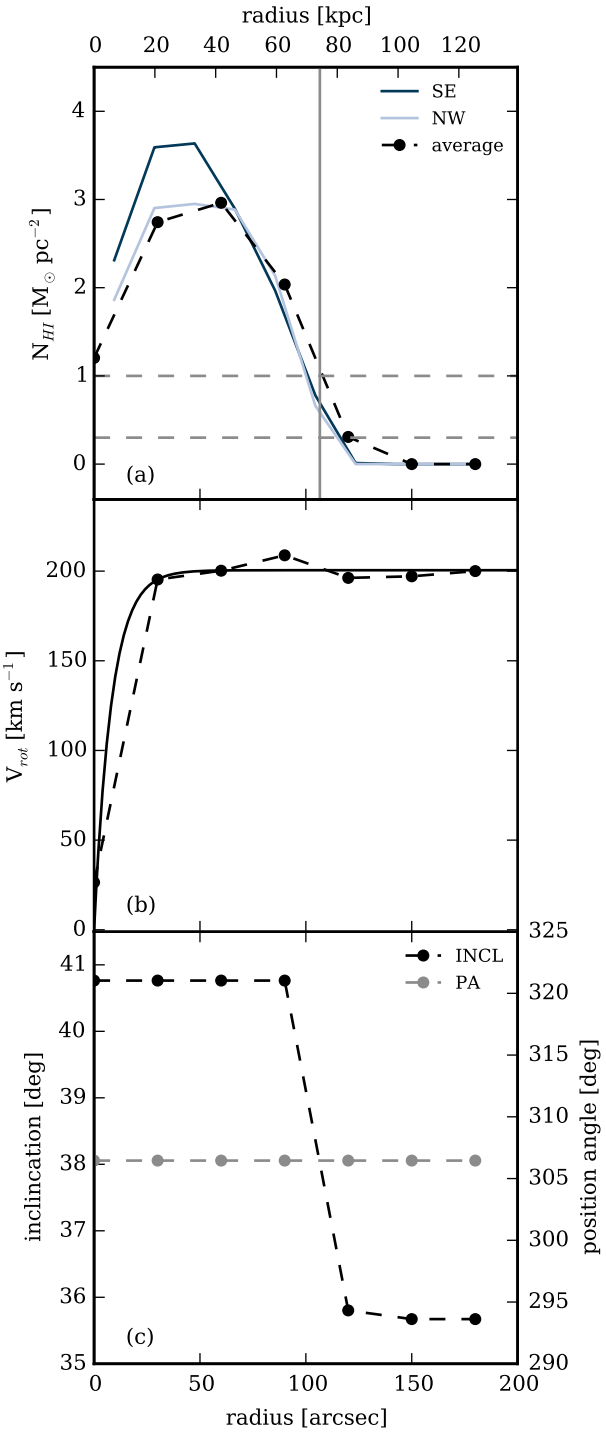

Figure 7. Radial profiles of HI properties: **(a):** The radial H I column density profile of ESO075-G006 in azimuthally averaged rings (black points and dashed line) and along the major axis from the centre going north-westerly (south-easterly) in light (dark) blue lines. The bottom grey dashed line marks the lower limit on column densities of $0.4 \cdot 10^{20}$ cm^{-2}, the top grey dashed line marks the 1 $M_\odot$ pc^{-2} level. The vertical grey, solid line marks the measured R_{HI}. **(b):** Rotation curve from TiRiFiC, the black dashed line connects the measurements and the black solid line is a fit to the data. **(c):** The radial variation of the inclination (black) and the position angle (grey) as fitted by TiRiFiC.

Figure 8 shows selected channel maps of the input data and resulting model cube. The model performs especially well in the velocity range between 10521 and 10721 km s^{-1}. More elaborate models have not been able to decrease the residuals in channels 10501 km s^{-1}.

5.4 Stability of ESO075-G006's disc

Combining the results of the TiRiFiC fit with radial profiles of H I and stellar mass, a global stability parameter can be determined for ESO075-G006 following Obreschkow & Glazebrook (2014); Obreschkow et al. (2016).

H I and stellar masses are calculated in elliptical concentric annuli. Inclination and position angle for each annulus are taken from the TiRiFiC result. For high sensitivity, the H I mass map is measured from a moment 0 map created from the robust=0.5 data cube without clipping. For the stellar masses, luminosities are measured from 2MASS K-band images and converted to stellar masses again following equation (3) in Wen et al. (2013). Together with the TiRiFiC measurement of the rotation curve, the integrated specific baryonic angular momentum calculated by:

$$j_B = \frac{\sum_i (M_{HI,i} + M_{\star,i}) \cdot V_{rot,i} \cdot r_i}{\sum_i (M_{HI,i} + M_{\star,i})}. \quad (5)$$

$M_{HI,i}$ and $M_{\star,i}$ are the H I and stellar mass and $V_{rot,i}$ the rotation velocity in the ith annulus with radius r_i. Equation 5 assumes that stars and H I rotate at the same speed.

The global stability parameter is then calculated by:

$$q = \frac{j_B \cdot \sigma}{G \cdot M_B} = \frac{8922\,\mathrm{km\,s^{-1}\,kpc} \cdot 11.2\,\mathrm{km\,s^{-1}}}{G \cdot 10^{11.2\pm0.1}\,M_\odot} \quad (6)$$

where G is the gravitational constant. We find $q = 0.16 \pm 0.02$. In Figure 9 the atomic to baryonic mass fraction is shown as a function of q. The data point for ESO075-G006 agrees with the analytic model by Obreschkow et al. (2016). This model assumes a flat, exponential disc, where gas is converted into stars when it is not Toomre-stable (Toomre 1964) and gas is stabilised by the specific baryonic angular momentum of the disc. For ESO075-G006 this implies, that the star formation efficiency is decreased by the relatively high specific baryonic angular momentum of the disc. The galaxy is therefore able to build up and support a very massive H I disc. It is still an H I excess galaxy for its optical luminosity. For its specific baryonic angular momentum, however, it hosts a normal amount of H I.

The angular momentum of the molecular gas was not included in this analysis, as no measurements are available. We argue, however, that the molecular gas does not contribute significantly to the baryonic angular momentum as most of the molecular gas will be located at small radii and the estimated molecular gas mass is smaller than both the H I and the stellar mass.

For comparison, we also show the data for THINGS galaxies (Walter et al. 2008; Obreschkow & Glazebrook 2014; Obreschkow et al. 2016), the only sample of massive galaxies for which this detailed analysis has been performed. We furthermore estimate the stability parameter for those HIghMass galaxies, for which a rotation velocity and a exponential scale length or a 25 mag arcsec^{-2} isophotal radius has been published. For this estimate the stellar specific angular momentum is calculated following equations (4) and

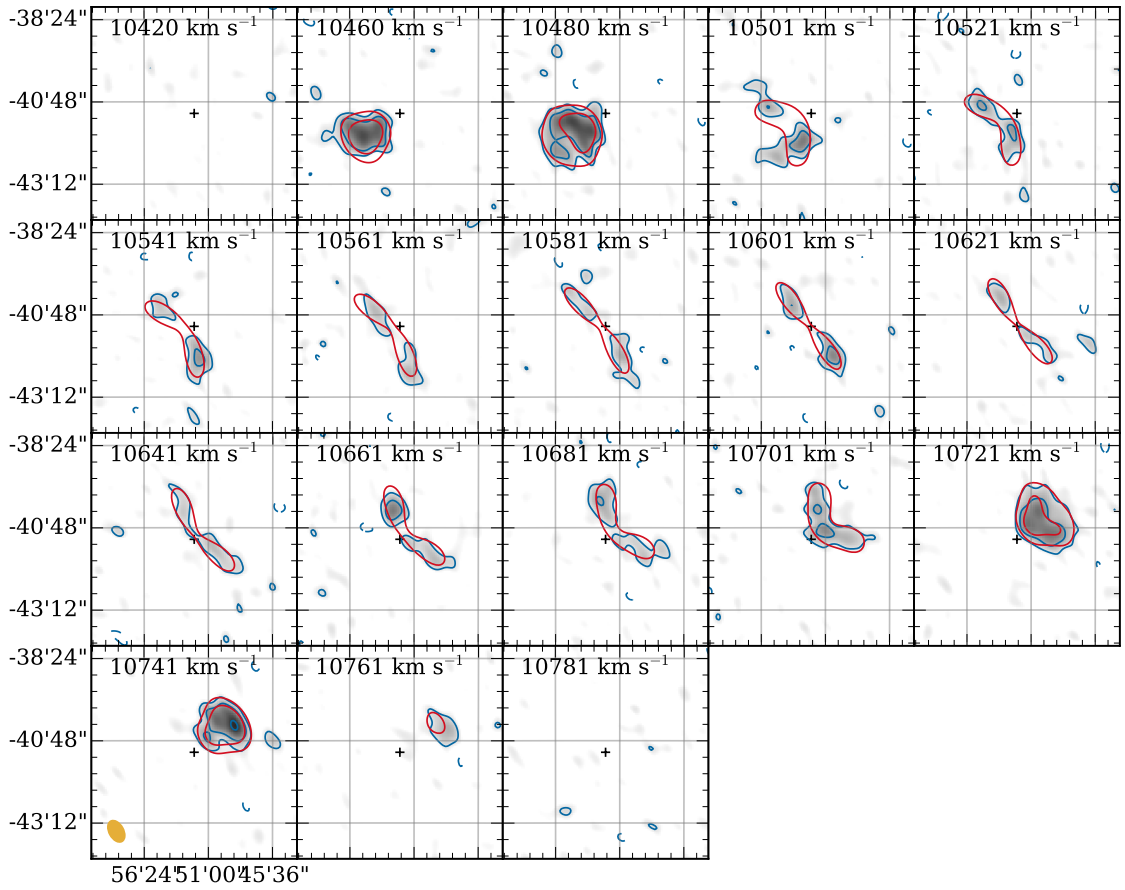

Figure 8. A selection of single channel maps from the H I data cube of ESO075-G006 (blue contours) overlaid on the grey scale image of the channel. The red contours show the TiRiFiC fit to the data. Both sets of contours are (-3.6, 3.6, 7.2, 14.4) mJy beam^{-1}. The velocity of each channel is given in the upper left corner. The black cross marks the centre of the galaxy. The coordinates are the same in all channels. For simplicity only minutes and seconds in the first panel are given.

(6) in Obreschkow & Glazebrook (2014). The specific angular momentum of the atomic gas is assumed to be twice the stellar specific angular momentum. For the baryonic specific angular momentum, these estimates are combined using Equation 5. Except for AGC 248881, the HighMass galaxies follow the model. The outlier is located in close proximity to other massive galaxies and its kinematics might therefore be altered. Encouraged by the success of this model to explain the extremely high H I mass of ESO075-G006 and HighMass galaxies, we will further populate this graph and test the model with the remaining HIX and control galaxies in the future.

5.5 The local environment of ESO075-G006

The data cube has been searched for dwarf galaxies and remnants thereof. A candidate for such a dwarf galaxy is the object to the north-west of the ESO075-G006. Arp & Madore (1987) have classified this galaxy together with ESO075-G006 as an interacting double.

Following the Hyper-Leda convention the companion is identified as PGC 277784 (Paturel et al. 2003) and is classified as a non-star object in the Guide Star Catalogue (GSC, Lasker et al. 2008). The coordinates of this object are: 21h 23′ 16.0″ −69° 40′ 25″. Assuming this companion is located at the same distance as ESO075-G006, a stellar mass can be estimated from the 2MASS K-band magnitude (taken from the 2MASS point source catalogue, Cutri et al. 2003). This yields $\log \mathrm{M}_\star[\mathrm{M}_\odot] = 9.0$.

Including the stellar mass of the dwarf in the stability analysis in the previous section does not change the q parameter significantly. To do so, we assumed that the dwarf would travel at the same rotation velocity as the surrounding H I.

No separate H I content is detected for PGC 277784 above the column density limit within the data cube. Assuming this dwarf to be an unresolved point source at the three sigma column density limit and to have a velocity width of 50 km s^{-1}, the upper limit for its H I mass is $\log \mathrm{M_{HI}/M_\odot} \leq 8.7$. With the estimated stellar mass this is equivalent to $\log \mathrm{f_{HI}} = -0.5$, which is well below the 1 σ scatter of the HIPASS running average in Figure 3.

The residual data cube of the TiRiFiC fit, i.e. the difference between the input data cube and the output TiRiFiC

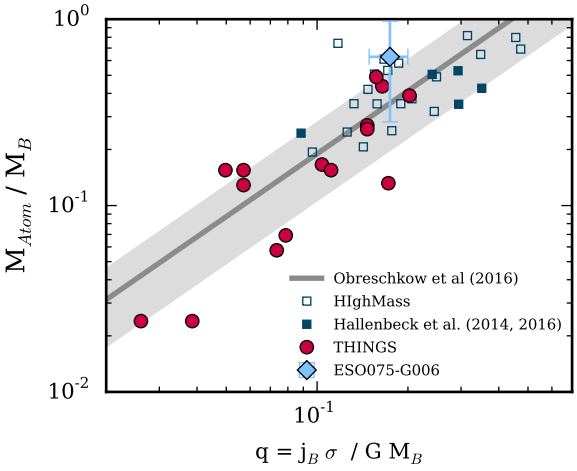

Figure 9. The atomic to baryonic mass fraction as a function of the global stability parameter q. The blue diamond presents our measured data for ESO075-G006. The red circles present the data of THINGS galaxies (Walter et al. 2008) as measured by Obreschkow & Glazebrook (2014). The black line and grey shaded area mark the analytical model by Obreschkow et al. (2016). Blue squares present HIghMass galaxies. Filled square indicate galaxies for which resolved H I maps have been published (Hallenbeck et al. 2014, 2016).

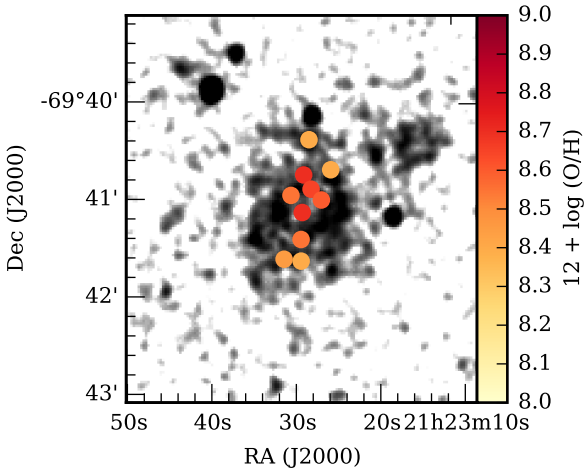

Figure 10. The gas-phase oxygen abundance distribution in ESO075-G006: The grey shaded image in the background is the *GALEX NUV* image. The coloured circles indicated star forming regions within which a metallicity has been measured. The colour of the circle indicates the measure metallicity.

model cube, does not reveal excess emission in the area of PGC 277784. Hence, there is no H I emission within the data cube that can not be explained with the warped H I disc model. It is to be noted though that the spatial resolution is limited and could be too coarse to detect signs of the companion.

No signature of other galaxies are found within an H I data cube of 1 deg in side-length and $V_{sys} \pm 600\,km\,s^{-1}$.

The nearest, similarly sized neighbour of ESO075-G006 is 2MASX J21200298 − 6924152, which is at a larger projected distance than 1 Mpc and its recession velocity differs by 600 km s^{-1}. Crook et al. (2007) does not place ESO075-G006 in a group. In summary, ESO075-G006 appears as an isolated field galaxy.

5.6 Optical spectra of ESO075-G006

We observed ESO075-G006 with three different WiFeS pointings along the ridge of the bar. For each of these pointings one stellar population model has been fitted to the median stacked spectra of all spaxels in the pointing, the recession velocity has been measured from the redshift of the Hα line and gas phase oxygen abundances have been measured for all star forming regions, in which the necessary lines for metallicity estimation have been detected.

Using the results of the stellar population modelling, a recession velocity of the stellar disc at each pointing has been measured. Furthermore, the redshift of the Hα line in all Voronoi bins indicates the rotation of the ionised gas component. All three components, i. e. stars, atomic and ionised gas are co-rotating. This indicates that the disc of ESO075-G006 has not been recently (less than one orbital time) disturbed by any major merger.

From the emission lines in the WiFeS data cubes metallicities can be measured as explained in Section 3.6. In Figure 10 those observed (star forming) regions, in which the four necessary emission lines have been detected, are circled. For these region a gas-phase oxygen abundance has been estimated.

The central metal abundance in the bar amounts to 12 + log(O/H) = 8.7. For a comparison we take the Sloan Digital Sky Survey data release 7 (SDSS, DR7, Abazajian et al. 2009) in a similar redshift range as the HIX galaxies. The stellar mass for these galaxies were taken from the MPA-JHU catalogue[9]. From these data we select all those galaxies that lie within $10.4 \leq \log M_\star[M_\odot] \leq 10.6$ and estimate the metallicity the same way as for ESO075-G006 from emission lines. The average and standard deviation of all estimated metallicities is $12 + \log(O/H) = 8.7 \pm 0.1$. Hence, the central gas–phase oxygen abundance of ESO075-G006 is average for its stellar mass.

In the four regions located on the outer spiral arms / the outer ring, the metallicity amounts to $12 + \log(O/H) = 8.4 \pm 0.1$. Moran et al. (2012) investigated the radial profiles of gas-phase oxygen abundance using the same metallicity estimator. In the same stellar mass range as ESO075-G006, they find the metallicity in some galaxies to drop as low as in ESO075-G006 but most galaxies are more metal rich in the outskirts (see figure 4 of Moran et al. (2012)). They further find a relation between the H I mass fraction and the metallicity in the outskirts of a galaxy (see figure 8 of Moran et al. (2012)). For $\log f_{HI} > 0.0$, they observe the metallicity in the outskirts to drop to values around 8.3, which is similarly metal poor as the outskirts of ESO075-G006. This result, however should be taken with caution as the relation between outer metallicity and $\log f_{HI} > 0.0$ is only sparsely sampled in Moran et al. (2012) and no reliable measurement of r_{90} is available for ESO075-G006. Hence, the location of outskirts in ESO075-G006 might be different than in the Moran et al. (2012) galaxies.

[9] http://www.mpa-garching.mpg.de/SDSS/DR7/

6 DISCUSSION

In the following, the results from Section 4 and 5 will be discussed. We will start with the discussion of ESO075-G006 then continue on to setting the HIX galaxies into context.

6.1 ESO075-G006

The aim of the detailed examination of ESO075-G006 has been to investigate the origin of the H I excess. As indicated in the introduction we are considering H I excess to due both clumpy and smooth accretion as well as due to inefficient star formation. In our data set we can search for evidence for any of following processes:

(i) non-circular gas motions due to inflowing gas or a lag of the thick disc as produced by a Galactic Fountain.
(ii) gas-phase metallicity gradients or inhomogeneities as gas accreted from the intergalactic medium is metal-poor. Metallicity inhomogeneities might coincide with star forming regions, which were triggered by the accretion event (Ceverino et al. 2016; Filho et al. 2013).
(iii) lopsided H I morphologies as filaments of cold gas accretion are distributed randomly.
(iv) signs of recent mergers, which would disturb both the H I and the stellar disc.
(v) a high angular momentum or other factors that reduce the star formation efficiency (Obreschkow & Glazebrook 2014; Leroy et al. 2008).

The hypothesis that ESO075-G006 went through a recent gas-rich major merger can be dismissed, because both the morphology and the velocity field are very regular and the stellar, atomic and ionised gas components are co-rotating.

Furthermore, H I richness purely due to a gas-rich minor merger with the dwarf companion in the north-west is also disfavoured. We find no evidence of this dwarf hosting its own distinct gas reservoir. The upper limit for the H I mass of the dwarf is $\log M_{HI}[M_\odot] \leq 8.7$, the difference between the measured and expected H I mass of ESO075-G006 is $\log M_{HI}[M_\odot] \leq 10.6$. Hence, the detection upper limit in H I mass of the dwarf is two orders of magnitudes too small to explain ESO075-G006's H I excess.

If the H I reservoir of PGC 277784 has already been incorporated into the H I disc of ESO075-G006, we can estimate the amount of H I brought in by PGC 277784 from its stellar mass and the gas mass fraction - stellar mass relation (see Figure 3). If PGC 277784 used to be an average HIPASS galaxy, this would result in $\log f_{HI} = 0.3$, which is equivalent to an H I mass of $\log M_{HI}/M_\odot = 9.3$. This is still more than an order of magnitude too small to explain the entire H I excess mass. Hence, there needs to be an additional reason for the H I excess of ESO075-G006. It is possible, however, that interaction with PGC 277784 is responsible for the small warp, as the warp occurs at similar galactocentric radii as the location of PGC 277784.

Our best-fitting TIRIFIC model does not need any radial gas motions or vertical velocity gradients to explain the velocity field of ESO075-G006. This implies that accretion or a Galactic Fountain could only operate at smaller column densities or spatial scales than can be detected in the H I data of ESO075-G006. Hence, H I excess due to a recent phase of violent cosmological accretion as well as a very active Galactic fountain can not be confirmed. We find, however, that the gas–phase oxygen abundance drops in the outskirts of ESO075-G006. In general, metallicity gradients are attributed to accretion of pristine, cosmological gas (e. g. Moran et al. 2012). Stevens et al. (2016a) find in the hydrodynamical, cosmological EAGLE simulations that hot halo gas already takes on the structure of the disc before it is accreted on the disc. If hot halo gas accretion is the dominant accretion channel in ESO075-G006, it would therefore be near impossible to detect signs of accretion in the morphology and kinematics of the galactic disc. One possible scenario might therefore be that ESO075-G006 is accreting gas but at low column densities or from the hot halo rather than through filaments.

An explanation for the massive H I disc of ESO075-G006 is provided by the global stability parameter (Obreschkow et al. 2016). Due to its high specific baryonic angular momentum, ESO075-G006 is able to stabilise the gas against star formation. A potential scenario for ESO075-G006 is that gas is constantly accreted over time. Due to the high stability of the disc, however, ESO075-G006 was not able to convert the accreted gas efficiently into stars as it is accreted and the massive H I disc built up over time. A similar scenario is suggested for HIghMass galaxy UGC 12506 (Hallenbeck et al. 2014) and Malin 1 (Boissier et al. 2016).

The reason for the high specific angular momentum can only be speculated about. Possible scenarios are that either ESO075-G006 has been formed in a dark matter halo at the high-spin tail of the halo spin distribution, ESO075-G006 has accreted angular momentum e. g. through accretion from filaments that were aligned with the galaxy rotation or ESO075-G006 simply has not lost any angular momentum over time. The semi-analytic simulation Dark-SAGE (Stevens et al. 2016b) suggest that the angular momentum of galaxies in the local universe is not determined by the angular momentum of the host halo. Current hydrodynamic simulations suggest that galactic discs lose angular momentum in major mergers (Lagos et al. 2016) and galactic winds increase the angular momentum (Genel et al. 2015). As ESO075-G006 is very isolated it might have never encountered any major merger, in which it could have lost angular momentum. It might have furthermore gone through an epoch of very active star formation, which in turn will have increased galactic winds and the angular momentum of the disc.

At the current SFR and without any further gas accretion, it would take ESO075-G006 approximately 15 Gyr to return onto the Dénes et al. (2014) scaling relation. So, unless, the H I disc of ESO075-G006 gets significantly stripped, it is likely to continue be an H I excess galaxy for a very long time.

6.2 HIX galaxies in context

The HIX galaxies have been selected to have a high H I mass in comparison to their *R*-band luminosity. For most HIX galaxies, this also implies a high H I mass fraction at a given stellar mass.

Comparing the H I based star formation efficiency of the HIX and control sample suggests that HIX galaxies form stars systematically less efficiently than the control sample.

The stellar mass range, the morphology and the specific SFR (sSFR) of HIX galaxies is similar to these properties of the control galaxies. This is important as Brown et al. (2015) have identified the H I mass fraction as a primary driver for sSFR as well as a residual relation with morphology and stellar mass. So, if the control and the H I rich sample match in these properties, the difference in H I content arises from other causes. Therefore, the comparison of this control to the HIX sample will enable us to investigate possible recent gas accretion events and answer the questions on where the excess gas has come from and why the excess gas has not yet been converted into stars.

We will address these questions in subsequent papers, in which we will investigate the H I disc and the distribution of the gas-phase oxygen abundance of the HIX galaxies in greater detail.

7 CONCLUSIONS

In this work we present the HIX galaxy survey targeting the most H I massive galaxies for their *R*-band luminosity. We find that these galaxies are normal star forming spirals for their stellar mass. However, their H I disc is more massive than in a control sample and they are inefficient at converting this gas reservoir into stars.

The most extreme galaxy in the sample is ESO075-G006. Making use of tilted ring fits to ATCA H I interferometric data combined with gas-phase metallicity information from WIFES optical IFU spectra, we find that this galaxy has not recently undergone major or violent accretion events but appears to be accreting at low levels. Its H I excess can, however, be attributed to a very high specific angular momentum, which prevents accreted gas from being transported to the centre of the disc and converted into stars. Comparing the current star formation rate of ESO075-G006 to the amount of excess gas suggests that unless ESO075-G006 loses H I in other processes than star formation at the current rate, it will continue be an H I excess galaxy for a very long time.

ACKNOWLEDGMENTS

We would like to thank the anonymous referee for helpful comments that improved the paper.

We would like to thank K. Gereb, D. Obreschkow, A. R. H. Stevens, D. Vohl, K. Glazebrook, M. Duree, J. Wang and Y. Bahe for insightful discussions and S. Forsayeth for outstanding computer support.

This research bases on data taken with the Australian Telescope Compact Array which is funded by the Commonwealth of Australia for operation as a National Facility managed by CSIRO. This is a large project with the project number C2705. We would like to thank the ATCA staff for excellent support during the observations.

KAL is supported by a CSIRO OCE Science Leader funded PhD top-up scholarship.

BC is the recipient of an Australian Research Council Future Fellowship (FT120100660). BC and LC acknowledge support from the Australian Research Council's Discovery Projects funding scheme (DP150101734).

The Parkes telescope is part of the Australia Telescope which is funded by the Commonwealth of Australia for operation as a National Facility managed by CSIRO.

This research has made use of the VizieR catalogue access tool, CDS, Strasbourg, France.

This publication makes use of data products from the Wide-field Infrared Survey Explorer, which is a joint project of the University of California, Los Angeles, and the Jet Propulsion Laboratory/California Institute of Technology, funded by the National Aeronautics and Space Administration.

This publication makes use of data products from the Two Micron All Sky Survey, which is a joint project of the University of Massachusetts and the Infrared Processing and Analysis Center/California Institute of Technology, funded by the National Aeronautics and Space Administration and the National Science Foundation.

This publicatio is based on observations made with the NASA Galaxy Evolution Explorer. GALEX is operated for NASA by the California Institute of Technology under NASA contract NAS5-98034.

This research has made use of SAOImage DS9, developed by Smithsonian Astrophysical Observatory.

This research has further made use of python packages, which are provided by the community. Not explicitly mentioned in the main body of this work are: astropy (Astropy Collaboration et al. 2013), NumPy[10] (van der Walt et al. 2011), SciPy[11] (Jones et al. 2001), matplotlib[12] (Hunter 2007) and APLpy[13].

REFERENCES

Abazajian K. N., et al., 2009, ApJS, 182, 543
Arp H. C., Madore B., 1987, A catalogue of southern peculiar galaxies and associations
Astropy Collaboration et al., 2013, A&A, 558, A33
Barnes D. G., et al., 2001, MNRAS, 322, 486
Bigiel F., Blitz L., 2012, ApJ, 756, 183
Bogdán Á., et al., 2015, ApJ, 804, 72
Boissier S., et al., 2016, A&A, 593, A126
Broeils A. H., Rhee M.-H., 1997, A&A, 324, 877
Brown T., Catinella B., Cortese L., Kilborn V., Haynes M. P., Giovanelli R., 2015, MNRAS, 452, 2479
Cappellari M., 2009, preprint (arXiv:0912.1303)
Cappellari M., Copin Y., 2003, MNRAS, 342, 345
Cappellari M., Emsellem E., 2004, PASP, 116, 138
Catinella B., Cortese L., 2015, MNRAS, 446, 3526
Catinella B., et al., 2010, MNRAS, 403, 683
Catinella B., et al., 2012, A&A, 544, A65
Catinella B., et al., 2013, MNRAS, 436, 34
Ceverino D., Sánchez Almeida J., Muñoz Tuñón C., Dekel A., Elmegreen B. G., Elmegreen D. M., Primack J., 2016, MNRAS, 457, 2605
Chabrier G., 2003, PASP, 115, 763
Childress M. J., Vogt F. P. A., Nielsen J., Sharp R. G., 2014, Ap&SS, 349, 617
Cluver M. E., et al., 2014, ApJ, 782, 90

[10] http://www.numpy.org/
[11] https://www.scipy.org/
[12] http://matplotlib.org/
[13] https://aplpy.github.io/

Crook A. C., Huchra J. P., Martimbeau N., Masters K. L., Jarrett T., Macri L. M., 2007, ApJ, 655, 790
Cutri R. M., et al., 2003, 2MASS All Sky Catalog of point sources.
Cutri R. M., et al., 2013, Technical report, Explanatory Supplement to the AllWISE Data Release Products
Davé R., Katz N., Oppenheimer B. D., Kollmeier J. A., Weinberg D. H., 2013, MNRAS, 434, 2645
Dénes H., Kilborn V. A., Koribalski B. S., 2014, MNRAS, 444, 667
Di Teodoro E. M., Fraternali F., 2014, A&A, 567, A68
Dopita M., Hart J., McGregor P., Oates P., Bloxham G., Jones D., 2007, Ap&SS, 310, 255
Doyle M. T., et al., 2005, MNRAS, 361, 34
Filho M. E., et al., 2013, A&A, 558, A18
Forbes J. C., Krumholz M. R., Burkert A., Dekel A., 2014, MNRAS, 438, 1552
Fraternali F., Sancisi R., Kamphuis P., 2011, A&A, 531, A64
Genel S., Fall S. M., Hernquist L., Vogelsberger M., Snyder G. F., Rodriguez-Gomez V., Sijacki D., Springel V., 2015, ApJ, 804, L40
Gentile G., et al., 2013, A&A, 554, A125
Giovanelli R., et al., 2005, AJ, 130, 2598
Hallenbeck G., et al., 2014, AJ, 148, 69
Hallenbeck G., et al., 2016, preprint, (arXiv:1610.03859)
Hambly N. C., et al., 2001a, MNRAS, 326, 1279
Hambly N. C., Irwin M. J., MacGillivray H. T., 2001b, MNRAS, 326, 1295
Haynes M. P., Giovanelli R., Chincarini G. L., 1984, ARA&A, 22, 445
Heald G., 2015, in Ziegler B. L., Combes F., Dannerbauer H., Verdugo M., eds, IAU Symposium Vol. 309, Galaxies in 3D across the Universe. pp 69–72 (arXiv:1409.7599), doi:10.1017/S1743921314009338
Heald G., et al., 2011, A&A, 526, A118
Huang S., et al., 2014, ApJ, 793, 40
Hughes T. M., Cortese L., Boselli A., Gavazzi G., Davies J. I., 2013, A&A, 550, A115
Hunter J. D., 2007, Computing in Science Engineering, 9, 90
Jones E., Oliphant T., Peterson T., et al., 2001, SciPy: Open source scientific tools for Python, http://www.scipy.org/
Józsa G. I. G., Kenn F., Klein U., Oosterloo T. A., 2007, A&A, 468, 731
Kim J.-h., Lee J., 2013, MNRAS, 432, 1701
Koribalski B. S., et al., 2004, AJ, 128, 16
Krumholz M. R., Burkhart B., 2016, MNRAS
Lagos C. d. P., Theuns T., Stevens A. R. H., Cortese L., Padilla N. D., Davis T. A., Contreras S., Croton D., 2016, preprint, (arXiv:1609.01739)
Lasker B. M., et al., 2008, AJ, 136, 735
Lauberts A., Valentijn E. A., 1989, The surface photometry catalogue of the ESO-Uppsala galaxies
Lee C., Chung A., Yun M. S., Cybulski R., Narayanan G., Erickson N., 2014, MNRAS, 441, 1363
Lemonias J. J., Schiminovich D., Catinella B., Heckman T. M., Moran S. M., 2014, ApJ, 790, 27
Leroy A. K., Walter F., Brinks E., Bigiel F., de Blok W. J. G., Madore B., Thornley M. D., 2008, AJ, 136, 2782
Maddox N., Hess K. M., Obreschkow D., Jarvis M. J., Blyth S.-L., 2015, MNRAS, 447, 1610
Mannucci F., Cresci G., Maiolino R., Marconi A., Gnerucci A., 2010, MNRAS, 408, 2115
Marinacci F., Binney J., Fraternali F., Nipoti C., Ciotti L., Londrillo P., 2010, MNRAS, 404, 1464
Marinacci F., Fraternali F., Nipoti C., Binney J., Ciotti L., Londrillo P., 2011, MNRAS, 415, 1534
Martin D. C., et al., 2005, ApJ, 619, L1
Martin A. M., Papastergis E., Giovanelli R., Haynes M. P., Springob C. M., Stierwalt S., 2010, ApJ, 723, 1359
Masci F. J., Fowler J. W., 2009, in Bohlender D. A., Durand D., Dowler P., eds, Astronomical Society of the Pacific Conference Series Vol. 411, Astronomical Data Analysis Software and Systems XVIII. p. 67 (arXiv:0812.4310)
Meurer G. R., et al., 2006, ApJS, 165, 307
Meyer M. J., et al., 2004, MNRAS, 350, 1195
Monnier Ragaigne D., van Driel W., Schneider S. E., Jarrett T. H., Balkowski C., 2003, A&A, 405, 99
Moran S. M., et al., 2012, ApJ, 745, 66
Morrissey P., et al., 2007, ApJS, 173, 682
Obreschkow D., Glazebrook K., 2014, ApJ, 784, 26
Obreschkow D., Glazebrook K., Kilborn V., Lutz K., 2016, ApJ, 824, L26
Oosterloo T., Fraternali F., Sancisi R., 2007, AJ, 134, 1019
Paturel G., Petit C., Prugniel P., Theureau G., Rousseau J., Brouty M., Dubois P., Cambrésy L., 2003, A&A, 412, 45
Pettini M., Pagel B. E. J., 2004, MNRAS, 348, L59
Pickering T. E., Impey C. D., van Gorkom J. H., Bothun G. D., 1997, AJ, 114, 1858
Saintonge A., et al., 2016, MNRAS, 462, 1749
Sánchez Almeida J., Elmegreen B. G., Muñoz-Tuñón C., Elmegreen D. M., 2014, A&A Rev., 22, 71
Sancisi R., Fraternali F., Oosterloo T., van der Hulst T., 2008, A&A Rev., 15, 189
Sault R. J., Teuben P. J., Wright M. C. H., 1995, in Shaw R. A., Payne H. E., Hayes J. J. E., eds, Astronomical Society of the Pacific Conference Series Vol. 77, Astronomical Data Analysis Software and Systems IV. p. 433 (arXiv:astro-ph/0612759)
Schiminovich D., et al., 2010, MNRAS, 408, 919
Schlegel D. J., Finkbeiner D. P., Davis M., 1998, ApJ, 500, 525
Schmidt T. M., Bigiel F., Klessen R. S., de Blok W. J. G., 2016, MNRAS, 457, 2642
Skrutskie M. F., et al., 2006, AJ, 131, 1163
Stevens A. R. H., Lagos C. d. P., Contreras S., Croton D. J., Padilla N. D., Schaller M., Schaye J., Theuns T., 2016a, preprint, (arXiv:1608.04389)
Stevens A. R. H., Croton D. J., Mutch S. J., 2016b, MNRAS, 461, 859
Toomre A., 1964, ApJ, 139, 1217
Vazdekis A., Sánchez-Blázquez P., Falcón-Barroso J., Cenarro A. J., Beasley M. A., Cardiel N., Gorgas J., Peletier R. F., 2010, MNRAS, 404, 1639
Walter F., Brinks E., de Blok W. J. G., Bigiel F., Kennicutt Jr. R. C., Thornley M. D., Leroy A., 2008, AJ, 136, 2563
Wang J., et al., 2013, MNRAS, 433, 270
Wang J., et al., 2014, MNRAS, 441, 2159
Wang J., Koribalski B. S., Serra P., van der Hulst T., Roychowdhury S., Kamphuis P., Chengalur J. N., 2016, MNRAS, 460, 2143
Wen X.-Q., Wu H., Zhu Y.-N., Lam M. I., Wu C.-J., Wicker J., Zhao Y.-H., 2013, MNRAS, 433, 2946
Wilson W. E., et al., 2011, MNRAS, 416, 832
Wong O. I., Meurer G. R., Zheng Z., Heckman T. M., Thilker D. A., Zwaan M. A., 2016, MNRAS, 460, 1106
Wright E. L., et al., 2010, AJ, 140, 1868
Zwaan M. A., et al., 2004, MNRAS, 350, 1210
van de Voort F., Schaye J., Booth C. M., Dalla Vecchia C., 2011, MNRAS, 415, 2782
van den Bergh S., 1962, AJ, 67, 486
van der Walt S., Colbert S., Varoquaux G., 2011, Computing in Science Engineering, 13, 22

This paper has been typeset from a TEX/LATEX file prepared by the author.